

An experimental study on the motion of buoyant particles in the free-surface vortex flow

Duinmeijer, Alex; Clemens, Francois

DOI

[10.1080/00221686.2020.1845827](https://doi.org/10.1080/00221686.2020.1845827)

Publication date

2021

Document Version

Accepted author manuscript

Published in

Journal of Hydraulic Research

Citation (APA)

Duinmeijer, A., & Clemens, F. (2021). An experimental study on the motion of buoyant particles in the free-surface vortex flow. *Journal of Hydraulic Research*, 59(6), 947-962.
<https://doi.org/10.1080/00221686.2020.1845827>

Important note

To cite this publication, please use the final published version (if applicable).
Please check the document version above.

Copyright

Other than for strictly personal use, it is not permitted to download, forward or distribute the text or part of it, without the consent of the author(s) and/or copyright holder(s), unless the work is under an open content license such as Creative Commons.

Takedown policy

Please contact us and provide details if you believe this document breaches copyrights.
We will remove access to the work immediately and investigate your claim.



An experimental study on the motion of buoyant particles in the free-surface vortex flow

Alex Duinmeijer & Francois Clemens

To cite this article: Alex Duinmeijer & Francois Clemens (2021) An experimental study on the motion of buoyant particles in the free-surface vortex flow, Journal of Hydraulic Research, 59:6, 947-962, DOI: [10.1080/00221686.2020.1845827](https://doi.org/10.1080/00221686.2020.1845827)

To link to this article: <https://doi.org/10.1080/00221686.2020.1845827>



Published online: 15 Jan 2021.



Submit your article to this journal [↗](#)



Article views: 107



View related articles [↗](#)



View Crossmark data [↗](#)

Research paper

An experimental study on the motion of buoyant particles in the free-surface vortex flow

ALEX DUINMEIJER (IAHR Member), PhD Student, *Water Management Department, Faculty of Civil Engineering and Geosciences, Delft University of Technology, the Netherlands/Engineering consultancy Municipality of Rotterdam, the Netherlands*
Email: s.p.a.duinmeijer@rotterdam.nl (author for correspondence)

FRANCOIS CLEMENS , Senior Researcher, Professor, *Unit of Hydraulic Engineering, Deltares, the Netherlands; Water Management Department, Faculty of Civil Engineering and Geosciences, Delft University of Technology, the Netherlands*
Email: francois.clemens@deltares.nl/f.h.l.r.clemens@tudelft.nl

ABSTRACT

Experiments are conducted in a Ø600 mm tank to analyse the 3D motion of buoyant particles in the free-surface vortex flow. The experiments revealed two stages in the particle motion: stage 1 is the helical motion along the vortex air core and stage 2 is the axial motion inside the vortex core. The stage 1 motion is sensitive to the particle's initial conditions by showing a chaotic behaviour and quantified by determining the largest Lyapunov exponent. Consequently, the predictability (forecast horizon) of the particle's motion is limited. A motion parameter is proposed that indicates if a continuous downward motion along the air core occurs. The dynamics in the stage 2 motion is determined by the imbalance between the particle's buoyancy force and fluid drag force. The drag appears to be determined by the Taylor column drag force as present in rotating fluids. Based on this force, a motion condition is proposed that indicates if axial motion inside the vortex core occurs.

Keywords: 3D-PTV; free-surface vortex; particle dynamics; chaotic behaviour; stable limit cycle; vortex core; axial particle motion; Taylor column drag coefficient

1 Introduction

The work described in this article is a part of a research project on the application of a free-surface vortex for the downward transport of floating particles; see the previous published article in this journal (Duinmeijer, Oldenziel, et al., 2019). To study the vortex's transport potential, an experimental set-up was built to generate vortices and to study the vortex driven motion of buoyant particles. The characteristic dimension L of the particles is 0.02–0.04 m and the Reynolds particle number is $\sim 10^2 < R_p < \sim 10^4$ with R_p defined as $(|V - U|) L/\nu$ where V and U are the flow and particle velocities respectively and ν the fluid's kinematic viscosity. The experimental results revealed two stages in the motion of the particles (Fig. 1). Stage 1 is characterized by the particle following a helical motion along the vortex air core until the particle reaches the air core bottom where the particle centralizes in the vortex core. During the downward motion the particle may be ejected out of the air core or reach a more or less stable orbit around the vortex air core at

a specific height. Stage 2 motion is the axial motion inside the vortex core where the particle is centralized in the core.

1.1 Problem definition

The vortex driven motion of buoyant particles is determined by the interaction between the particle dynamics and the flow characteristics.

The stage 1 motion (helical motion along the air core) is determined by the inertial and lift forces (F_L) acting on the particle. Over the last decades many studies have been reported on the motion of bodies in shear and rotating flows in which the generation of F_L is involved. Saffman (1965, 1968) and Mei (1992) studied the F_L on a sphere in a shear flow for $1 \ll R_p \leq 10^2$. Auton (1987) studied the F_L on a fixed sphere in an inviscid weak shear flow. Auton et al. (1988) studied the forces on a moving sphere in an inviscid rotational flow. For $10 < R_p < 10^2$, Bagchi and Balachandar (2002) studied the lift coefficient C_L of a sphere in a linear shear and a vor-

Received 17 October 2019; accepted 19 August 2020/Currently open for discussion.

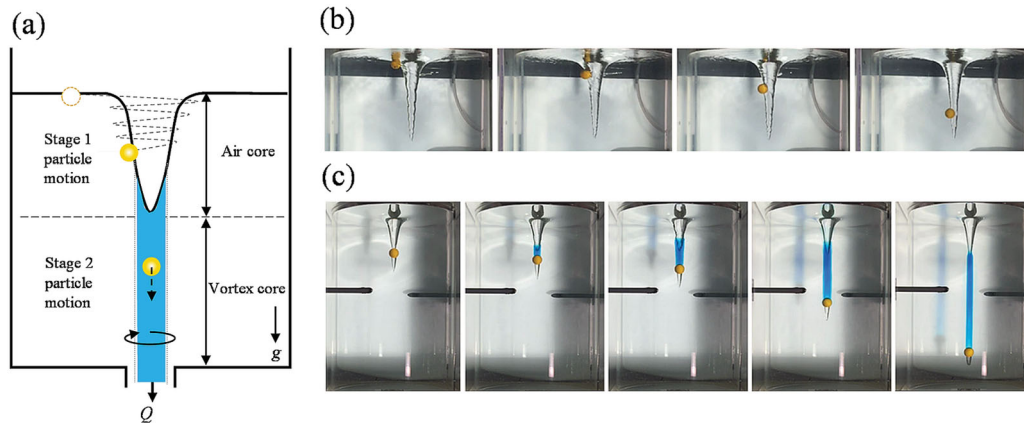


Figure 1 (a) Definition of the observed stages in the vortex driven motion of buoyant particles. The stage 1 motion is the helical motion along the air core. The stage 2 motion is the axial motion inside the vortex core. (b) Stage 1 motion of a Ø38 mm sphere. (c) Stage 2 motion of a Ø38 mm sphere

text flow. Van Nierop et al. (2007) studied the F_L on a Ø1 mm air bubble in a solid-body rotating flow for $0.01 < R_p < 500$. Bluemink et al. (2009) examined the C_L for a freely rotating Ø8 mm sphere in a solid-body rotating flow for $2 \leq R_p \leq 1060$. Fukada et al. (2014) studied the forces acting on a sphere that generate the sphere's rotation in both irrotational and solid-body rotating flow for $5 < R_p < 10^2$. Voßwinkel (2017) studied the vortex transportability for Ø3 to Ø40 mm spheres. Based on experimental data, Voßwinkel determined correlations between downward motion, the hydraulic conditions and particle characteristics. However, the characteristics of the vortex flow field are not considered and so the outcome of the research is limited to one intake geometry only.

The stage 2 motion (axial motion inside the vortex core) is determined by the fluid axial drag force $F_{D,z}$ and the buoyancy force. The motion parallel to the axis of a solid-body rotating fluid induces a complex phenomenon described by Proudman (1916) and Taylor (1917). They found that a moving sphere was accompanied by a fluid column that circumscribed the sphere and determined the drag on the sphere. For inviscid flow, Stewartson (1952) presented a study on the drag force of the Taylor column and proposed an expression for this force. For a low viscous fluid, Moore and Saffman (1968) studied the $F_{D,z}$ on a rising body with a Taylor column circumscribing the body. Maxworthy (1970) reported an experimental study on $F_{D,z}$ for Ø12.7 and Ø19 mm rising spheres along the centre axis of a Ø305 mm rotating tank for $\sim 5 < R_{p,z} < \sim 10^3$, with $R_{p,z}$ the particle axial Reynolds number $|V_z - U_z| L/\nu$ with V_z and U_z the axial fluid and particle velocity respectively. Tanzosh and Stone (1994) studied the particle motion parallel to the axis of rotating fluid for $R_{p,z} \ll 1$. Bush et al. (1994) performed a survey of particle motion in solid-body rotating fluids for motions parallel and perpendicular to the axis of rotation. Bush et al. (1995) presented an experimental and theoretical study on the axial motion of a bubble in a solid-body rotating fluid.

The stage 1 motion in this study mostly occurs in the irrotational part of the vortex flow, while the literature mentioned

mainly focuses on the motion in rotational flows, e.g. solid-body rotating flow. Hence, there is a lack of data on particle motion in irrotational flows. For the stage 2 motion, the axial motion is not driven by a buoyancy force but instead by a non-uniform axial flow. Furthermore, the flow field is not fully in solid-body rotating but limited to a distance of $\sim r_c$ from the vortex centre axis with r_c the vortex core radius. Consequently, the results from the literature are not directly applicable to studying the vortex driven motion of buoyant particles in both stages.

1.2 Goal and outline of this paper

To obtain experimental data on the vortex driven motion of buoyant particles, an extensive experimental and theoretical study is conducted for both stage 1 and stage 2 particle motion. In this article the results of this study are presented. The outline is as follows. Section 2 addresses the experimental set-up and programme. Section 3 describes the results of the study on the stage 1 motion and Section 4 presents the results on the stage 2 motion. The conclusions and recommendations of this study are formulated in Section 5.

2 Experimental set-up and programme

2.1 Experimental set-up

The experimental setup consists of an acrylic tank with an inside diameter of 0.610 m and a height of 1 m. The experimental particles are released on the water surface at variable or fixed position. The 3D motion is determined by a 3D particle tracking velocimetry (PTV) set-up. For a more detailed description of the set-up, the reader is referred to Duinmeijer, Moreno-Rodenas, et al. (2019). In several experiments, the particle only showed a 2D motion at the free-surface. For these combinations of characteristics, additional 2D-PTV experiments were done. The 2D-PTV set-up consists of an IO Industries Flare 2M280CCX high speed camera placed above the water surface. The experimental

Table 1 Experimental particle characteristics

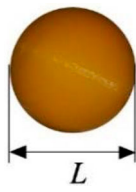

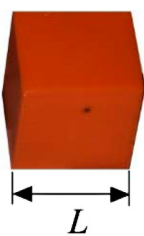
Particle no.	Shape and characteristic dimension L	Dimension	Density
71	Sphere 	Ø20 mm	$692 \pm 1 \text{ kg m}^{-3}$
83		Ø38 mm	$630 \pm 1 \text{ kg m}^{-3}$
84			616 kg m^{-3}
86			$709 \pm 2 \text{ kg m}^{-3}$
88			$665 \pm 2 \text{ kg m}^{-3}$
91		Ø19 mm	675 kg m^{-3}
92			600 kg m^{-3}
101		Ø25 mm	$771 \pm 5 \text{ kg m}^{-3}$
102			$730 \pm 5 \text{ kg m}^{-3}$
103			$860 \pm 3 \text{ kg m}^{-3}$
111	Ovoid 	$76 \times 38 \times 19 \text{ mm}$	$787 \pm 1 \text{ kg m}^{-3}$
113		$L = 38 \text{ mm}$	$666 \pm 1 \text{ kg m}^{-3}$
114			$859 \pm 2 \text{ kg m}^{-3}$
123		$38 \times 19 \times 9.5 \text{ mm}$	$875 \pm 2 \text{ kg m}^{-3}$
124		$L = 19 \text{ mm}$	$973 \pm 4 \text{ kg m}^{-3}$
141	Cube 	$30.6 \times 30.6 \times 30.6 \text{ mm}$	$746 \pm 2 \text{ kg m}^{-3}$
143			$914 \pm 1 \text{ kg m}^{-3}$
144			$859 \pm 1 \text{ kg m}^{-3}$
153		$20.2 \times 20.2 \times 20.2 \text{ mm}$	$923 \pm 2 \text{ kg m}^{-3}$
154			$869 \pm 4 \text{ kg m}^{-3}$
156			$895 \pm 3 \text{ kg m}^{-3}$

Table 2 Experimental series of vortex characteristics

Series	Q ($\text{m}^3 \text{ h}^{-1}$)	Γ_∞ ($\text{m}^2 \text{ s}^{-1}$)	r_c (mm)	H_D (m)	Series	Q ($\text{m}^3 \text{ h}^{-1}$)	Γ_∞ ($\text{m}^2 \text{ s}^{-1}$)	r_c (mm)	H_D (m)
1	0.69	0.07	8.6	0.09	5	1.50	0.16	16.2	0.17
2	0.69	0.08	9.7	0.10	6	1.50	0.23	17.9	0.26
3	1.16	0.12	8.2	0.24	7	2.50	0.31	15.3	0.54
4	1.16	0.17	9.8	0.35	8	2.50	0.44	17.3	0.85

particles are produced using 3D-printing technology and come in three shapes: sphere, ovoid and cube (Table 1). The particles were designed with different density ρ_p to quantify the effect of this parameter on the particle's dynamics. The uncertainty in ρ_p is determined to be in a range of $1\text{--}5 \text{ kg m}^{-3}$.

2.2 Experimental programme and procedure

The 3D-PTV experimental programme comprises eight series of vortex characteristics and 15 particles. The 2D-PTV programme consists of six series of vortex characteristics (series 1 and 3–7) and five spheres. The vortex characteristics are the bulk circulation Γ_∞ , the core radius r_c and the air core depth H_D (Table 2). The vortex characteristics and the 3D-flow field are determined by stereo particle image velocimetry (SPIV) (Duinmeijer, Oldenziel, et al., 2019). The 3D-PTV and 2D-PTV experiments were repeated five times and two times respectively to check the

reproducibility of the experiment. The particles were released on the surface with a remote-controlled device for the 3D-PTV experiments and by hand for the 2D-PTV experiments. For the stage 1 motion and when the particles showed a repetitive motion, the sequence was recorded more than once to check the consistency of this behaviour. For the stage 2 motion, the experiment was finished when either one of the following conditions was applied: (1) the particle disappeared through the outlet within $t_a < \sim T$ and (2) the particle was still in the control volume at $t_a > \sim T$. Experiments meeting condition 1 are labelled as “Motion” and experiments meeting condition 2 are labelled as “No motion”. t_a is the measured time needed for a particle to travel the distance from the air core bottom to the outlet: $H - H_D$. T is a characteristic time parameter and determined by the hydraulic conditions: $T = (H - H_D)/U_{z,\min}$ with $U_{z,\min}$ a defined minimum required particle velocity. By definition, $U_{z,\min}$ is set to 0.01 m s^{-1} and thus $T = 100(H - H_D)$.

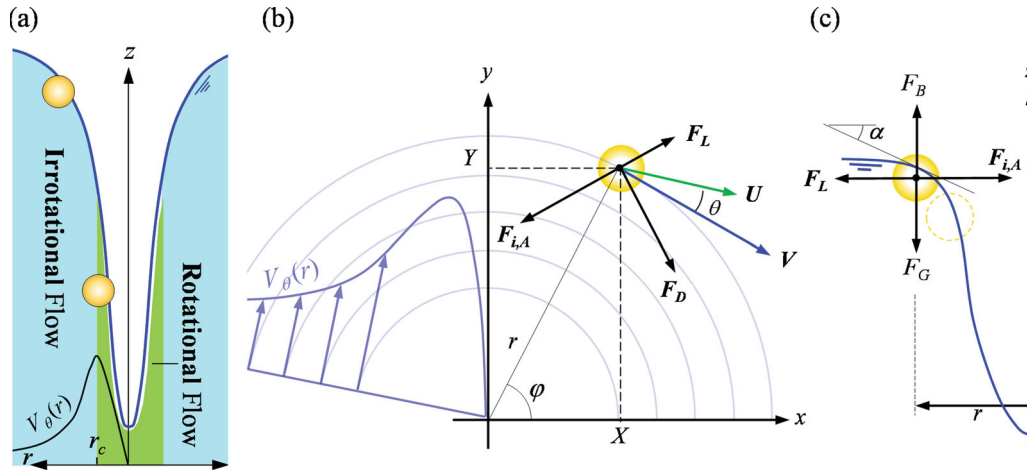


Figure 2 (a) Illustration of particle motion through two types of flow. (b) Motion in the horizontal plane. The left side shows a schematic profile of $V_\theta(r)$. (c) Motion in the vertical plane along the air core

3 Study on the stage 1 motion: the helical motion along the vortex air core

It was found that most experiments are not repeatable which is an indication of a chaotic behaviour in the particle’s dynamics. To study and quantify this behaviour, Section 3.1 addresses the development of a simplified model to describe the particle’s motion in the horizontal plane. In Sections 3.2 and 3.3 the chaotic dynamics of both experimental and model results are presented. In Section 3.4 a motion parameter Φ is proposed for a downward motion along the air core and Section 3.5 finally discusses the results.

3.1 Model for the particle’s dynamics

Defined in a right handed Cartesian coordinate system (Fig. 2), and based on the Lagrangian approach, a set of nonlinear particle motion equations describing the particle’s dynamics are numerically solved using a trust-region-dogleg algorithm (e.g. Powell, 1970). The validity of the applied equations for a viscid rotating flow is discussed in Section 3.5. For an internal frame of reference, the generalized equation of motion for a body with volume χ at moderate to large Reynolds numbers moving in a non-uniform flow is (e.g. Bluemink et al., 2009; Tio et al., 1993; Van Nierop et al., 2007):

$$(\rho_p + C_A \rho_f) \chi \frac{dU}{dt} = F_{i,A} + F_D + F_L + F_g \quad (1)$$

The history, or Basset, force is considered to be insignificant for $R_p > 5$ (Van Nierop et al., 2007) and is therefore neglected as in this study $10^2 < R_p < 10^4$. $F_{i,A}$ is the inertial/added mass force and due to the acceleration of the unperturbed fluid at the sphere’s centre:

$$F_{i,A} = \rho_f (1 + C_A) \chi \frac{DV}{Dt} = \rho_f (1 + C_A) \chi \frac{\partial V}{\partial t} + V \cdot \nabla V \quad (2)$$

with $DV/Dt = \partial V/\partial t + V \cdot \nabla V$ the material derivative. The added mass coefficient C_A accounts for the fluid’s inertia close to the sphere with $C_A = 0.5$ for a submerged sphere in a fluid of infinite extent. For a floating sphere the effect of the free-surface is to decrease the C_A . For example, Berkite (1972) found for a sphere that $C_A \approx 0.4$ for $h/a = 1$ and $C_A \approx 0.19$ for $h/a = 0.5$ (applied here) with h the distance between the surface and the sphere’s centre. F_D is the drag force on a body moving through a fluid. For $R_p \gg 1$, this force is expressed by:

$$F_D = 0.5 \rho_f C_D A_N (V - U) (|V - U|) \quad (3)$$

The drag coefficient C_D is quantified by the expression suggested by Holzer and Sommerfeld (2008) and verified for $R_p \leq \sim 10^5$, covering the experimental range of this study:

$$C_D = \frac{24}{R_p} + \frac{3}{\sqrt{R_p}} + 0.42 \quad (4)$$

The hydrodynamic lift force F_L consists of two components: a force $F_{L,\omega}$ induced by the flow vorticity ω and a force $F_{L,\Omega}$ due to the particle’s rotation Ω_p (the ‘Magnus’ lift force). For $R_p \gg 1$, the vorticity lift force $F_{L,\omega}$ is (e.g. Auton et al., 1988 and Van Nierop et al., 2007):

$$F_{L,\omega} = \rho_f \chi C_L (V - U) \times \omega \quad (5)$$

with ω calculated by taking the curl of the velocity:

$$\omega = \nabla \times V \quad (6)$$

When considering only the z -component of ω , the horizontal lift force $F_{L,\omega}$ is:

$$F_{L,\omega} = \rho_f \chi C_L (V - U) \omega_z \quad (7)$$

A number of experimental and numerical studies determining the lift coefficient C_L depending on flow type are found in literature: Van Nierop et al. (2007) stated that the influence of

the sphere's rotation on C_L is significant and not addressed for $R_p \gg 1$. Bluemink et al. (2009) examined the effect of the sphere's rotation on C_L for $R_p \leq 200$ and proposed a linear decoupling of C_L in a flow vorticity contribution ($C_{L,\omega}$) and Magnus lift contribution ($C_{L,\Omega}$). Based on the latter study and valid for $R_p \gg 200$, $C_{L,\omega}$ is determined by:

$$C_{L,\omega} = 0.51^{10} \log(R_p) - 0.22 \quad (8)$$

The vorticity ω_z depends on the radius due to the viscous diffusion and is defined by Burgers' expression of $\omega_z(r)$ (Duinmeijer, Oldenziel, et al., 2019) and thus $F_{L,\omega}$ is:

$$F_{L,\omega} = \frac{\rho_f \chi C_{L,\omega} (V - U) \Gamma_\infty}{\pi r_c^2} \exp\left[-\left(\frac{r}{r_c}\right)^2\right] \quad (9)$$

Equation (7) is valid for a rotational flow with uniform ω_z . $\omega_z(r)$ is simplified and assumed to have a constant value which is the average $\bar{\omega}_z$ over at the sphere's diameter:

$$\bar{\omega}_z = \frac{1}{L} \int_{r-0.5L}^{r+0.5L} \omega(r) dr \quad (10)$$

The Magnus lift force $F_{L,\Omega}$ is generated by the particle's rotation Ω_p . For a sphere in an irrotational flow which rotates around its z -axis, the horizontal lift force $F_{L,\Omega}$ is determined with the potential flow theory and known as the Kutta–Joukowski lift theorem:

$$F_{L,\Omega} = 2\rho_f \chi (V - U) \Omega_p \quad (11)$$

with $(V - U)$ taken at the centre of the body. The particle's rotation is generated by a torque T_p due to an asymmetric stress

distribution along the particle surface. The equation of particle rotation motion is:

$$\frac{d\Omega_p}{dt} = \frac{a}{I_p} \int_{A_s} \tau_{a,\theta} dA_s = \frac{T_p}{I_p} \quad (12)$$

For a sphere in both a rotational and irrotational vortex flow, Fukada et al. (2014) proposed an expression for T_p as function of the streamline curvature κ :

$$T_p = \frac{\rho_f}{2} \left(\frac{L}{2}\right)^5 C_T (\Omega_{p,st} - \Omega_p) (|\Omega_{p,st} - \Omega_p|) \quad (13)$$

with $\Omega_{p,st}$ being the steady angular velocity:

$$\Omega_{p,st} = 0.0554\kappa (V - U) R_p^{0.635} \quad (14)$$

The torque coefficient C_T is:

$$C_T = 239 \left(\frac{L^2 (|\Omega_{p,st} - \Omega_p|)}{\nu}\right)^{-0.956} \quad (15)$$

Equations (14) and (15) are fitting equations for $R_p < 10^2$. The last forces are the body forces and limited to the gravity force F_g :

$$F_g = \chi (\rho_f - \rho_p) g \quad (16)$$

The model is validated by comparing the experimental particle motion with the model results. The initial particle conditions $X_{p,0}$ (position $x_{p,0}$, velocity $V_{p,0}$ and particle rotation $\Omega_{p,0}$) are based on measurements and serve as model-input data. Figure 3a–d shows a comparison between model and experimental results for experiments with a $\varnothing 38$ mm sphere. The

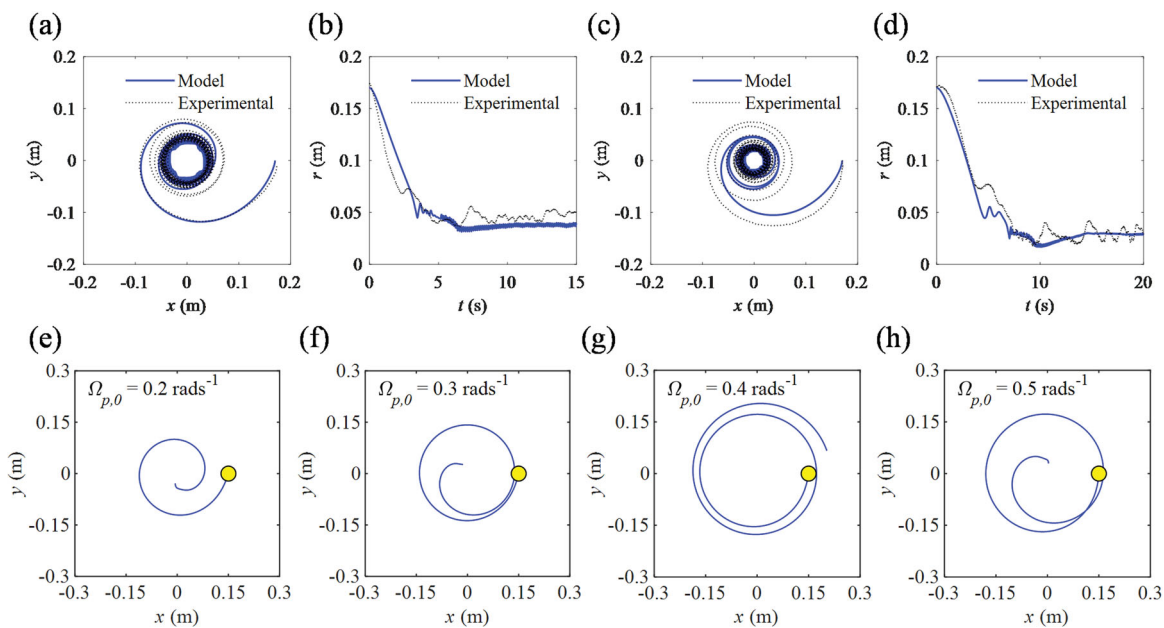


Figure 3 (a, b) Experimental and model particle trajectory and radial position of sphere 86 at series 6. (c, d) Results of sphere 86 at series 3. (e–h) Model trajectories as function of $\Omega_{p,0}$

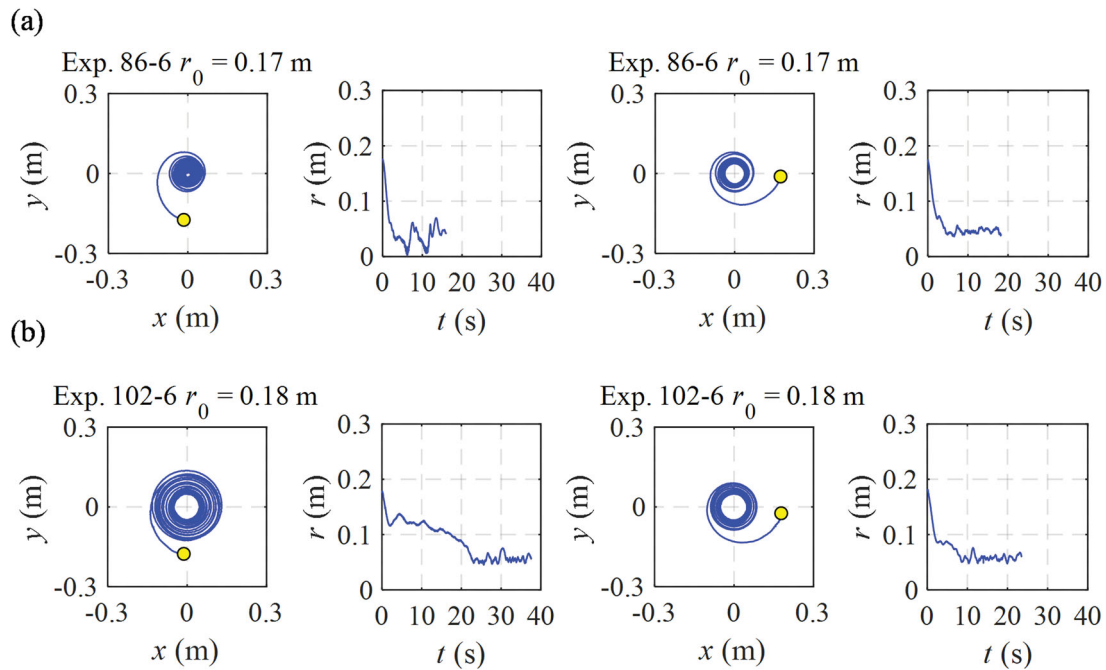


Figure 4 (a) Experimental trajectories and radial position of sphere 86 at series 6 with $x_0, y_0 = [0, -0.17]$ and $x_0, y_0 = [0.17, 0]$. (b) trajectories and radial position of sphere 102 at series 6 with $x_0, y_0 = [0, -0.18]$ and $x_0, y_0 = [0.18, 0]$

model shows a similarity with the experiments in the sense that both the experiments and the model show that the particle ends up in either a stable limit cycle at a more or less constant radial distance r or the particle ends up in the vortex core. However, in detail and for small time scales, the model differs significantly with the experimental results as discussed in Section 3.5. Although the proposed model is a simplification in many aspects, it shows that the observed non-repeatability of the experiments may find its explanation in the nonlinear dynamic (chaotic) nature of the studied system. This is illustrated in Fig. 3e–h which shows major changes in model trajectories due to minor changes in initial conditions.

3.2 Experimental results: limitations on the predictability of the particle motion

Analysis of the experimental horizontal particle trajectories conducted at controlled hydraulic conditions but with different initial particle positions $x_{p,0}$ in the flow field showed major differences between the trajectories. Consequently, there is a certain non-repeatable behaviour of the experiments. As an example, Fig. 4a shows the measured trajectories of a $\varnothing 38$ mm sphere. In the first experiment, the sphere is released at $[x_0, y_0] = [0 \text{ m}, -0.17 \text{ m}]$ and in the second experiment, the sphere is released at $[0.17 \text{ m}, 0 \text{ m}]$. In the first experiment, the sphere reaches the air core bottom after ~ 5 s and subsequently the sphere is ejected. In the second experiment, the sphere ends in a stable limit cycle at $r \approx 0.05$ m. Another obvious example of the non-repeatable behaviour is shown in Fig. 4b. In the first experiment, a $\varnothing 25$ mm sphere is released at $[0 \text{ m}, -0.18 \text{ m}]$ and in the second experiment at $[0.18 \text{ m}, 0 \text{ m}]$. Both experiments

show a stable limit cycle at $r \approx 0.05$ m but in the first experiment, this cycle is reached at $t \sim 8$ s where in the second experiment the cycle is reached at $t \sim 22$ s. This chaotic behaviour is not uncommon in nonlinear dynamical systems like the studied system. Chaotic behaviour is an important characteristic in relation to the predictability of the vortex driven particle motion. In the next section, the predictability of this system is analysed in detail.

3.3 Phase portrait, largest Lyapunov exponent and limitations to the predictability/forecast horizon

A phase portrait depicts the trajectories of a dynamical system. Each set of initial conditions is represented by a vector presenting the direction and magnitude of the systems change. Consequently, the portrait shows for a large ensemble of initial conditions the dynamic behaviour of the system. As portraits based on experiments are very time consuming and difficult to establish numerous combinations of initial conditions with slightly different values, the portraits presented here are constructed with the numerical model. The applied ensemble of initial conditions consists of the radial position r_0 from 0.02 to 0.30 m (step size 0.005 m), the radial velocity $U_{r,0}$ from -1.0 to 1.0 m s^{-1} (step size 0.1 m s^{-1}) and two rotations: $\Omega_{p,0} = 0$ and $\Omega_{p,0} = 1.5 \text{ rad s}^{-1}$. So, the portrait is made by an ensemble of 1056 different initial conditions. Figure 5a, b shows the phase portrait for sphere 86 ($\varnothing 38$ mm) and 5c, d for sphere 101 ($\varnothing 38$ mm). All figures includes several “trajectories” with the initial conditions illustrated by a blue dot. The portraits obviously show that, depending on the initial conditions, both spheres can move to a stable limit cycle. In the experiments, this

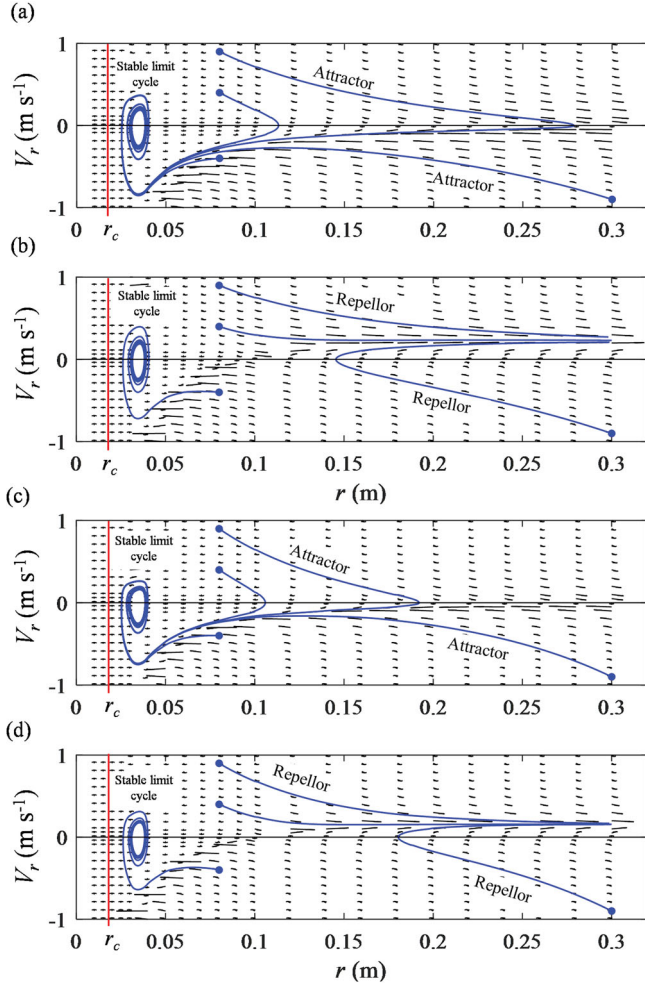


Figure 5 (a, b) Model phase-portraits for sphere 86 at series 6. (a) Results for $\Omega_{p,0} = 0 \text{ rad s}^{-1}$. (b) results for $\Omega_{p,0} = 1.5 \text{ rad s}^{-1}$. (c, d) Model phase-portraits for sphere 101 at series 6. (c) Results for $\Omega_{p,0} = 0 \text{ rad s}^{-1}$. (d) results for $\Omega_{p,0} = 1.5 \text{ rad s}^{-1}$

cycle is the stable orbit around the air core at an approximately constant height (e.g. Fig. 4b). This cycle attracts neighbouring trajectories and is defined as an *attractor*. On the other hand, the sphere can move in an unstable limit cycle with increasing radius and thus move outward of the centre. This cycle repels trajectories and is thus a *repellor*. In conclusion: the behaviour of the system is strongly influenced by the particle initial conditions and, indeed, the system shows chaotic behaviour that implies a limit to the system's forecast horizon. However, not all features seen in the experiments are reproduced by the model, which was to be expected given the simplifications made in the model.

The largest Lyapunov exponent: a quantification for the limited predictability/forecast horizon

For dynamical nonlinear systems that are sensitive to initial conditions as shown in the former sections, the predictability of a system is quantified by the largest Lyapunov exponent λ (LLE) that characterizes the separation rate of infinitesimally close

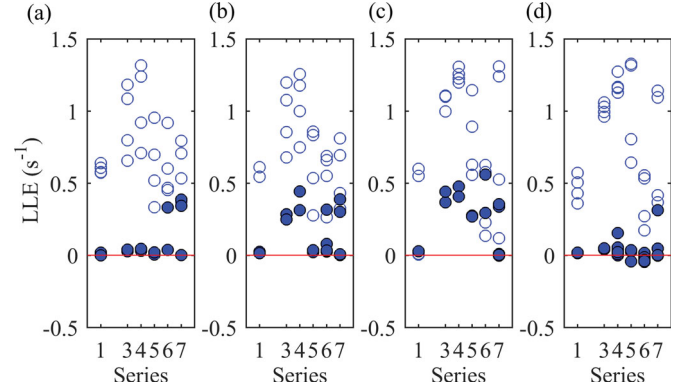


Figure 6 (a–d) LLEs of the experimental and model datasets of spheres 86, 88, 101 and 102 respectively. The filled and open circles represent the experimental and model data respectively. Differences between the results are due to the simplifications made in the model

trajectories starting with a small difference in initial condition $\delta \mathbf{X}_{p,0}$:

$$|\delta \mathbf{X}_p(t)| \approx e^{\lambda t} |\delta \mathbf{X}_{p,0}| \quad (17)$$

If $\lambda < 0$, the difference converges in time to zero which implies a stable system. If $\lambda > 0$, the difference increases in time which implies a “chaotic” and consequently a non-predictable system. The algorithm proposed by Rosenstein et al. (1993) is applied for the quantification of LLE and calculated for both the experimental and model results by applying an embedding dimension of $m = 3$. The model must use the experimental initial conditions $\mathbf{X}_{p,0}$ but these are not known in detail. The model LLEs are therefore calculated for four combinations of $\mathbf{X}_{p,0}$ that are assumed as realistic: $r_0 = 0.15 \text{ m}$, $\Omega_{p,0} = 0$ and 0.2 rad s^{-1} and $U_{\theta,0} = 0.5V_\theta$ and $0.99V_\theta$. Figure 6 shows the calculated LLEs. The experimental and model LLEs show the same trend and are in general > 0 . The differences between experiment and model LLEs are due to the simplifications made in the model. The inverse of the LLE (the Lyapunov time, $1/\lambda$) is a characteristic timescale indicating the forecast horizon of the particle motion. For the studied system, this range is ~ 0.8 to $\sim 10 \text{ s}$ and when compared to the timescale of 2 s for hydrodynamic chaotic oscillations (Gaspard, 2005), the system of particle motion in the free-surface vortex flow can be quantified as limited predictable.

3.4 Stage 1 motion parameter for downward motion along the air core

To ensure transport, a stage 1 motion parameter Φ is developed that indicates if downward motion along the air core occurs. The validity of Φ is discussed in Section 3.5. Φ is the ratio between the inertial/added mass force and the lift force: $\Phi = |\mathbf{F}_{i,A}| / (\mathbf{F}_{L,\omega} + \mathbf{F}_{L,\Omega})$. For a downward motion, the condition $\Phi > 1$ has to be met. This implies that the particle remains “pushed” against the air core until the bottom of the air core is reached. By application of Eqs (7), (9) and (11), while neglecting the

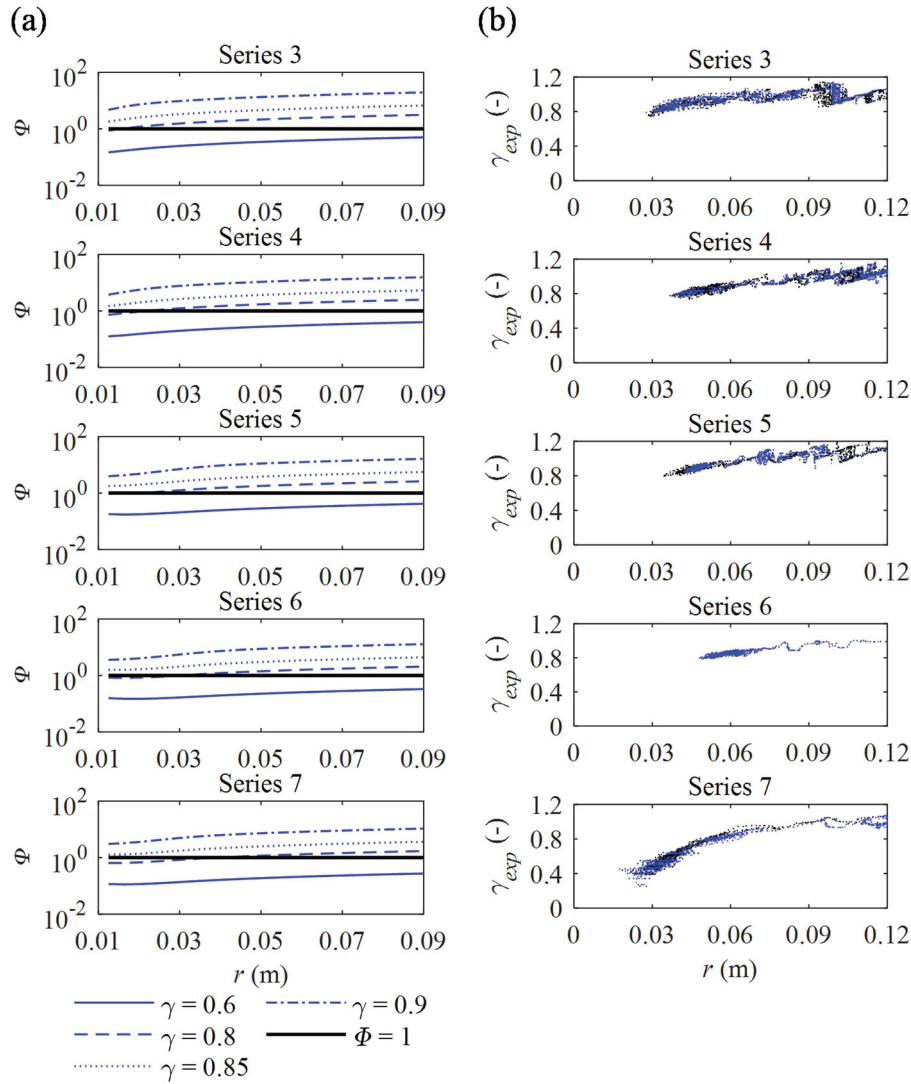


Figure 7 (a) Motion parameter Φ for $\varnothing 25$ mm sphere and series 3 to 7. A downward motion ($\Phi > 1$) is provided at approximately $\gamma > 0.8$. (b) Relative velocity parameter γ_{exp} during the sphere's downward motion and determined from two sets of 2D-PTV measurements

radial fluid velocity, Φ is:

$$\Phi = \frac{|\rho_f (1 + C_A) \chi (\mathbf{V} \cdot \nabla \mathbf{V})| \cdot \mathbf{e}_r}{\rho_f \chi (\mathbf{V} - \mathbf{U}) [2\Omega_p + C_L \omega_z] \cdot \mathbf{e}_r} \quad (18)$$

For a circular motion expressed in Cartesian coordinates with the sphere's centre positioned at $[x, 0]$, $V_x = 0$ and $V_y \partial V_x / \partial y = V_y^2 / x$. Furthermore, the particle velocity U_y in the relative velocity term $(V_y - U_y)$ is dynamic and has a limited predictability and thus is a priori unknown. Therefore U_y is expressed as γV_x with γ the relative velocity parameter: $(V_y - U_y) = V_y(1 - \gamma)$. Equation (18) is then expressed as:

$$\Phi = \frac{(1 + C_A) V_x^2}{x V_x (1 - \gamma) (2\Omega_p + 1.8\omega_z)} \quad (19)$$

The ω_z is a known function of x where Ω_p varies with time. Ω_p is therefore replaced by $\Omega_{p,sl}$ which is the maximum value at position x and thus a conservative approach. For a cylindrical

coordinate system and applying Burgers' (1948) model of V_θ , the motion parameter Φ is:

$$\Phi = \frac{0.76L^{-2}(1 - \gamma)^{-1} \left\{ 1 - \exp \left[-\left(\frac{r}{r_c}\right)^2 \right] \right\}}{\left(\frac{0.0054(\Gamma_\infty L)^{0.64}}{(1 - \gamma)^{1.64} r^{2.64} v^{0.64}} \left\{ 1 - \exp \left[-\left(\frac{r}{r_c}\right)^2 \right] \right\} \right)^{1.64} + \frac{0.57}{r_c^2} \exp \left[-\left(\frac{r}{r_c}\right)^2 \right]} \quad (20)$$

Given the vortex and particle characteristics, Φ gives an indication of the minimum required value of $\gamma(r)$ for a continuous downward motion. An example is provided for sphere 103 ($\varnothing 25$ mm) at series 3 to 7. Figure 7a shows Φ for $\gamma = 0.5, 0.8, 0.85$ and 0.9 . The results show that continuous downward motion occurs for $\gamma > \sim 0.8$. The validity of Φ is evaluated by analysing the experimental results and γ_{exp} where $\gamma_{exp}(r) = V_\theta(r)/U_\theta(r)$ with U_θ the measured value from the experiments. Figure 7b shows the results of γ_{exp} . The value of γ_{exp} is

shown during the sphere's downward motion. Indeed for series 3 to 6, the experiments show that downward motion is terminated at approximately $\gamma_{exp} < \sim 0.8$. At this position $\Phi \approx 1$ where the sphere detaches the air core. For series 7 downward motion is terminated at $\gamma_{exp} < 0.5$. This occurs mainly at unstable situations where the sphere "touches" the air core bottom ($r = 0$ m) but ends in a stable limit cycle with $\gamma_{exp} \approx 0.8$. To conclude, Φ provides an indication of downward motion along the air core occurs. However, the applicability depends on the correct quantification of γ , which is subject to further study.

3.5 Discussion

Given the simplifications and assumptions applied in formulating the model, the validity of this model and hence that of Φ derived from it has to be discussed.

A main model simplification is the absence of the air core. This "solid" boundary deaccelerates the horizontal motion towards the vortex centre, giving the lift force F_L more time to grow in magnitude. This can be observed in the model trajectories of Fig. 3a and c, showing a faster motion of the particle towards the centre. Another model characteristic is that the free-surface vortex is a 2D line vortex that contains an irrotational and a by approximation solid-body rotating flow field with the transition at $r \sim 2r_c$. So, the particle is subject to two types of flow (Fig. 2a) and even both types simultaneously at $r < \sim (r_c + 0.5L)$ with the particle's centre at r . The model is therefore limited to particle dimensions with $L \leq \sim 2r_c$. A third subject is the particle's influence on the surrounding flow field which is hard to quantify with experiments because of the particle dynamics. In the far field, say $r > 3r_c$, the (horizontal) flow has no restrictions to pass the sphere and mutual influence is assumed to be not significant and confined to a limited area directly around the sphere. In the region $r < 2r_c$, the approximately vertical air-water interface represents a restriction to the flow to pass and the mutual influence will be more significant. Consequently, the model results in the region $r < 2r_c$ must be interpreted with care.

The drag force F_D (Eq. 4) is based on an uniform flow. Bluemink et al. (2009) showed that Eq. (4) is also valid for a rotating flow with $\text{Re}_p < \sim 10^3$, $\sim 1/1.5L > \kappa > \sim 1/18L$ and vorticity parameter $\Omega L/V \leq 0.1$ with Ω the fluid's angular velocity. In this study vorticity (ω_z) is zero for $r > \sim 2r_c$. So, Eq. (4) is assumed as applicable for the sphere's position $r > \sim (r_c + 0.5L)$. The Magnus lift force $F_{L,\Omega}$ (Eq. 11) uses potential flow theory which is also applicable to the curved streamlines in the irrotational part of the vortex flow. However, the fluid in the presented study is not ideal and the boundary layer gives flow separation where the asymmetric downstream wake affects $F_{L,\Omega}$. Nevertheless, the potential flow approach gives a proper prediction of $F_{L,\Omega}$ and is applicable to this study for $r > \sim (r_c + 0.5L)$. The applied torque equation (Eq. 13) is determined for $5 \leq \text{Re}_p \leq 10^2$ and for streamline curvatures $\kappa < 1/30L$ where this study uses $10^2 \leq \text{Re}_p \leq 10^4$

and $\sim 1/L \leq \kappa \leq \sim 1/12L$. However, the study of Fukada et al. (2014) indicates that their findings are valid for a much higher range of Re_p and thus applicable to this study. The applicability of Eq. (14) for $\kappa > 1/30L$ is according to the knowledge of the authors unknown and a subject to further study. On the other hand and for $\kappa \gg 1/30L$, various experiments showed ejection of the sphere out of the air core due to unbalance between the inertial and lift forces. This was not predicted by the model which indicates that $\kappa \gg 1/30L$ does not result in unrealistic high values of $F_{L,\Omega p}$. Consequently, the applied expressions of F_D and $F_{L,\Omega p}$ are applicable for every sphere's position $r > \sim (r_c + 0.5L)$. As the motion parameter Φ is derived from the model, Φ is also applicable for $r > \sim (r_c + 0.5L)$. However, Φ uses the equation of steady $\Omega_{p,st}$ (Eq. 14) that gives the maximum lift forces for $r < \sim (r_c + 0.5L)$. This can be interpreted as a conservative approach which makes Φ applicable for all r .

Furthermore, it has to be noted that an exact replication of the experimental results by the model is not sought after in this study. The model is merely meant to support the hypothesis that a relatively simple feed-back mechanism (flow induced lift forces) may cause inherent unpredictable dynamics in the presented system.

4 Study on stage 2 motion: the axial motion inside the vortex core

This chapter addresses the study and quantification of the axial particle motion inside the vortex core. A stage 2 motion condition is developed to predict the axial motion. As the condition uses the axial velocity in the vortex core, Section 4.1 first addresses the characteristics of this velocity. Section 4.2 addresses the development of the motion condition. Section 4.3 discusses the results and applicability of the condition.

4.1 Axial velocity profile

The axial flow in the vortex core is found to be concentrated in a domain bounded by a radius in the order of $r \approx 2$ to $3 r_c$ as shown by the stereo PIV measurements of e.g. Duinmeijer, Oldenziel, et al. (2019). The velocity profile is Gaussian shaped with a maximum close to $r = r_c$. Figure 8 shows the SPIV measured axial velocities for series 1 to 7. The velocities are measured at three heights in the vortex tank (29, 49 and 62 cm above tank bottom). As the motion condition uses a uniform velocity, the first step is to approximate the measured $V_z(r)$ with a Gaussian function using the measured values of $V_{z,max,av}$ and r_{max} :

$$V_z(r) = V_{z,max,av} \exp \left[- \left(\frac{r - r_{max}}{\alpha r_{max}} \right)^2 \right] \quad (21)$$

$V_{z,max,av}$ is the averaged value of the measured $V_{z,max}$ at each height in the vortex, r_{max} the radial position of the maximum

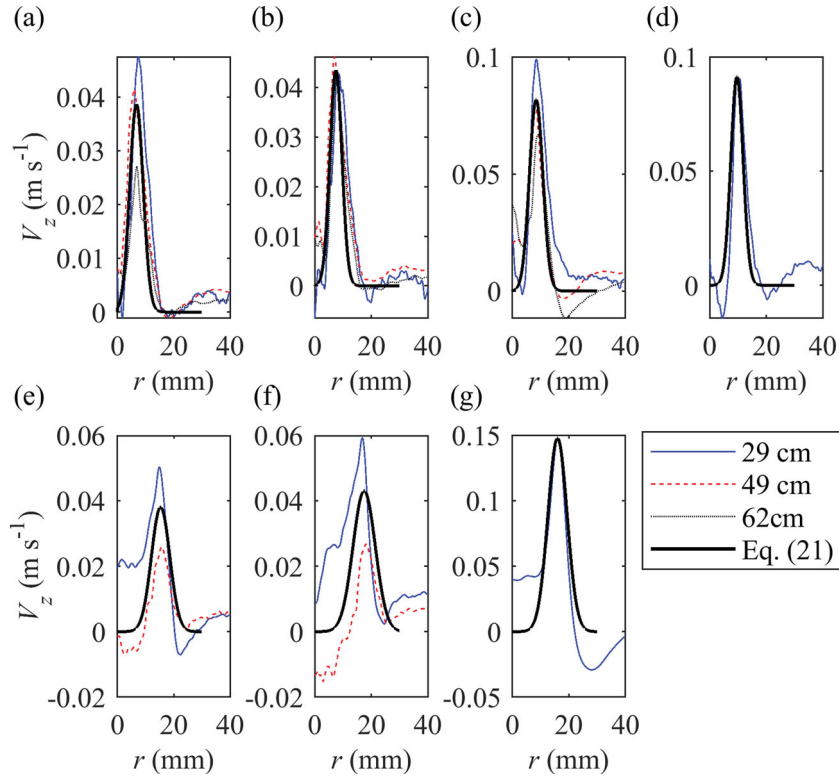


Figure 8 (a–g) Measured and approximated axial velocity profiles (thick line) for series 1 to 7 with $\alpha = 0.5, 0.4, 0.4, 0.32, 0.3, 0.32$ and 0.3

V_z and α the width factor of the profile for the best fit with the measured profiles (Fig. 8). The approximated $V_z(r)$ is assumed as uniform by using the average velocity \bar{V}_z over a radial domain equal to half the length of the particle that is centralized in de vortex core: $r = 0.5L$:

$$\bar{V}_z = \frac{1}{A} \iint_A V_z(r) dA_N = \frac{8}{L^2} \int_0^{0.5L} V_z(r) r dr \quad (22)$$

By applying Eq. (21), the plane averaged uniform velocity \bar{V}_z is then approximated by:

$$\bar{V}_z = \frac{8V_{z,max,av}}{L^2} \int_0^{0.5L} \exp \left[-\left(\frac{r - r_{max}}{\alpha r_{max}} \right)^2 \right] r dr \quad (23)$$

Consequently, the boundary conditions for \bar{V}_z are $L, V_{z,max,av}, r_{max}$ and α . The values of \bar{V}_z applied in this study are approximated inclusive the 95% confidence interval ($\pm 2\sigma$) with $\sigma = 0.002V_{\theta,max}$ (Westerweel & Scarano, 2005).

4.2 Stage 2 motion condition

This section addresses the development of the stage 2 motion condition. The first part addresses the results of a study applying the independent experimental parameters to predict axial motion. The second part addresses the development of the motion condition by applying the axial Navier–Stokes equation and the presence of a Taylor column.

Motion condition based on the independent experimental parameters

The independent experimental parameters in the experiments are H, Q, D, L, C_D, ρ_p and ρ_f . These parameters can be represented by two dimensionless parameters N_B and N_D . The first is the relative density and represents the effect of buoyancy on the axial particle motion:

$$N_B = \frac{\rho_f - \rho_p}{\rho_f} \quad (24)$$

N_D can be read as the axial drag force acting on the particle and generated by the axial flow velocity V_z :

$$N_D = \frac{Q^2 C_D}{D^2 H L^2 g} \quad (25)$$

The term $Q^2/(D^2 H)$ shows similarity to an axial velocity gradient $d\bar{V}_{z,i}/dz$ using the average axial outlet velocity $\bar{V}_{z,i}$. The C_D represents the effects of viscosity and particle shape. For the sphere, C_D is calculated with Eq. (4). For the cubes and ovoids, C_D is calculated with the correlation formula for non-spherical particles proposed by Holzer and Sommerfeld (2008) and verified for $R_p \leq \sim 10^5$:

$$C_D = \frac{8}{R_p} \frac{1}{\sqrt{\psi_\perp}} + \frac{16}{R_p} \frac{1}{\sqrt{\psi}} + \frac{3}{\sqrt{R_p}} \frac{1}{\psi^{3/4}} + 0.42 \cdot 10^{0.4(-\log \psi)^2} \frac{1}{\psi_\perp} \quad (26)$$

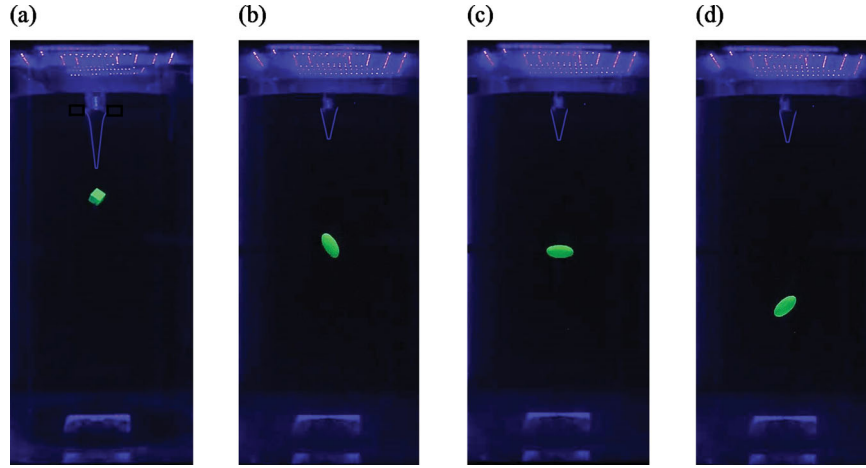


Figure 9 (a) Stationary orientation of an “angled” cube in the vortex core. (b–d) Dynamic orientation of ovoid in the vortex core

Ψ is the ratio between A_S of the volume-equivalent sphere and the non-spherical particle. Ψ_{\perp} is the ratio between the sphere’s A_N and the non-spherical particle. As both the cubes and ovoids are not point symmetric, the C_D depends on the particle’s orientation at the start of the axial motion along the vortex core with respect to the flow direction. This orientation is dynamic as shown in Fig. 9. The cubes show an angled stationary orientation with A_N a hexahedron with a rib length of $\frac{1}{2}\sqrt{2}L$ and so $A_N = 1.3L^2$. The initial orientation of the ovoids is taken as the averaged value of three orientations (calculations not given here). As a result, the C_D is:

$$\begin{aligned} \text{Angled cube : } C_D &= \frac{26.09}{R_p} + \frac{3.52}{\sqrt{R_p}} + 0.80 \\ \text{Ovoid : } \bar{C}_D &= \frac{26.32}{R_p} + \frac{3.58}{\sqrt{R_p}} + 0.88 \end{aligned} \quad (27)$$

As first assumption, C_D is taken as an approximated average over the experimental range of $R_{p,z}$. For the spheres, cubes and ovoids $C_D = 0.7, 1.1$ and 1.2 , respectively. Figure 10 shows

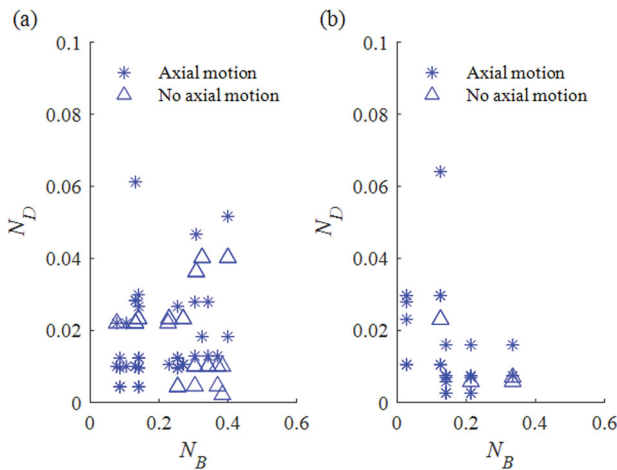


Figure 10 Experimental results of the measured motion of the particles as function of N_B and N_D . (a) Results for the spheres and cubes. (b) Results for the ovoid

the results of the 3D-PTV measured motion as function of N_B and N_D . The results are presented by the labels “Motion” and “No motion” as defined in Section 2.2. The results show no distinct relation between particle motion and the particle and vortex characteristics. Indeed, various experiments show the same values of N_B and N_D but with opposite results. There were no logical explanations found for the obtained results. Consequently, it seems not possible to describe the motion condition as a function of the experimental parameters H, Q, D, L, C_D, ρ_p and ρ_f .

Motion condition based on Taylor-column drag force

The axial motion is characterized by the following conditions: (1) the particle is centralized in the vortex core without radial motion ($U_r = 0$); (2) the axial flow is axi-symmetric ($\partial/\partial\theta = 0$), stationary ($\partial/\partial t = 0$) and defined as radial uniform ($\partial/\partial r = 0$); and (3) there is only vorticity in the z -direction. Using Eqs (1–3) and (16), the equation of axial particle motion is then:

$$\begin{aligned} (\rho_p + C_A\rho_f)\chi \left(\frac{\partial U_z}{\partial t} + U_z \frac{\partial U_z}{\partial z} \right) &= \rho_f (1 + C_A)\chi \left(V_z \frac{\partial V_z}{\partial z} \right) \\ &+ 0.5\rho_f C_D A_N (V_z - U_z)(|V_z - U_z|) + \chi(\rho_f - \rho_p)g \end{aligned} \quad (28)$$

The derivation of the motion condition focuses on the onset of particle motion and not on the particle motion itself. Therefore, the left term in Eq. (28) must be > 0 . Furthermore, at the onset of motion the term $(1 + C_a) V_z \partial V_z / \partial z$ is assumed to be much smaller than the buoyancy and drag force term and therefore neglected. The equation of motion then reduces to:

$$- 0.5\rho_f C_D A_N (V_z - U_z)(|V_z - U_z|) = \chi(\rho_f - \rho_p)g \quad (29)$$

which is the expected balance between the axial drag force and buoyancy force. The uniform velocity in the drag force expression is approximated by applying the radial uniform axial velocity \bar{V}_z as addressed in Section 4.1. In order to initiate a

motion along the vortex core, the following condition must be met:

$$\frac{0.5C_D A_N (\bar{V}_z - U_z)^2}{\chi g} = \frac{\rho_f - \rho_p}{\rho_f} \quad (30)$$

As mentioned in the introduction, a particle moving along the axis of a solid-body rotating fluid can be accompanied by a Taylor column circumscribing the particle. This column has a significant effect on the drag force. The criterion for Taylor column formation is expressed by the Rossby number $R_o = V_z/(\Omega 0.5L) < \sim 0.3$ with Ω the fluid angular velocity and $0.5L$ the radius of the sphere (Bush et al., 1994). In the present study, $R_o < \sim 0.03$ and the Taylor column is most likely to be present. Maxworthy (1970) experimentally studied the drag force on a rising sphere in a rotating flow. For large values of the Taylor number ($T_a > \sim 10^2$) representing the relative magnitude of the Coriolis force to viscous force:

$$T_a = \frac{\Omega(0.5L)^2}{\nu} \quad (31)$$

and for $N > 200$ that represents the relative magnitude of Coriolis force to inertia force:

$$N = \frac{2\Omega(0.5L)^2}{U_z} \quad (32)$$

Maxworthy found that the C_D for a sphere is independent of R_z and depends on N only. In this study, the expression $(0.5L)$ is used to indicate the use of the sphere radius. Based on experiments at $T_a > \sim 200$, that can be assumed as a geostrophic balanced fluid, Maxworthy (1970) found the following expression for the sphere's drag coefficient:

$$C_{D,Taylor} = (2.60 \pm 0.05) \left(\frac{2\Omega(0.5L)}{U_z} \right)^{1.00 \pm 0.01} \quad (33)$$

The results of Maxworthy (1970) are in line with the theoretical results for inviscid conditions as presented by Stewartson (1952) and Moore and Saffman (1969), which were $C_{D,Taylor} = 1.51N$. As the maximal tangential velocity V_θ occurs near the vortex core radius r_c , the (maximum) angular velocity Ω is by approximation:

$$\Omega(r_c) \approx \frac{V_\theta(r_c)}{r_c} \quad (34)$$

By using the validated Burger's vortex model for V_θ (i.e. Duijnmeijer, Oldenziel, et al., 2019), Ω is approximated by:

$$\Omega(r_c) \approx \frac{\Gamma_\infty}{2\pi r_c^2} \left\{ 1 - \exp \left[- \left(\frac{r_c}{r_c} \right)^2 \right] \right\} \approx \frac{0.32\Gamma_\infty}{\pi r_c^2} \quad (35)$$

The parameter N and thus $C_{D,Taylor}$ is than a function of the vortex characteristics Γ_∞ , r_c and L :

$$C_{D,Taylor} \approx 2.60N \approx \frac{1.66\Gamma_\infty(0.5L)}{\pi r_c^2(\bar{V}_z - U_z)} \quad (36)$$

By substituting $C_{D,Taylor}$ in Eq. (30), the following condition is obtained that indicates axial motion along the vortex core:

$$\frac{0.84\Phi_T\Gamma_\infty\bar{V}_z}{\pi r_c^2 g} \neq \frac{\rho_f - \rho_p}{\rho_f} \quad (37)$$

In fact, Eq. (37) expresses the condition for stage 2 motion along the vortex core as function of the vortex and particle characteristics. The left term presents the dimensionless Taylor drag force term $N_{D,Taylor}$:

$$N_{D,Taylor} = \frac{0.84\Phi_T\Gamma_\infty\bar{V}_z}{\pi r_c^2 g} \quad (38)$$

Φ_T is the Taylor drag shape factor: $\Phi_T = k(A_N/\chi)(0.5L)$. This factor is introduced because Eq. (33) is valid for spheres where this study also uses cubes and ovoids. k is a shape correction factor for the cubes and ovoids and defined as the ratio between the C_D of Eq. (27) and the sphere (Eq. 4). The cubes have a hexahedron shaped A_N , so, the integration domain to calculate \bar{V}_z is approximated with the average radius of the inner and outer circle circumscribing the hexahedron: $[0, 0.66L]$. The calculation of A_N for the ovoid is not given here. Figure 11 shows a nice example of the influence of dimension L on the downward particle motion. Compared to the $\emptyset 25$ mm sphere (Fig. 11a, b), the $\emptyset 38$ mm sphere (Fig. 11c, d) has a four times higher upward buoyance force but does show a downward motion. This is due to the significant higher \bar{V}_z over the spheres cross-sectional area A_N .

The $N_{D,Taylor}$ is validated with the experimental results. These results are presented by the labels "Motion" and "No motion" but supplemented with a label "Indecisive motion". This label represents experiments that show a downward motion but with $t_a > T$ and therefore not labelled as "Motion" (Section 2.2). The experimental uncertainty is 12% and defined as the percentage experiments labelled "Indecisive motion". Figure 12a, b shows the experimental and theoretical results for 66 spheres and cubes. The line $N_B = N_D$ represents the condition for "Motion" or "No motion". The calculations of $N_{D,Taylor}$ generally match with the experimental results but also reveal a few mismatches. Figure 12c, d shows the results for 31 ovoids. The results show an overprediction of $N_{D,Taylor}$. This is probably due to the disputable assumption that every orientation is subjected to an equal time distribution. In reality, the behaviour of the ovoid shows some similarity with the chaotic motion of an elliptical body due to body-vortex interactions as reported by Roenby and Aref (2010). Hence, it is difficult to provide a representative time distribution of each orientation.

4.3 Discussion

The predicted $N_{D,Taylor}$ generally matches with the experimental results but also reveals some mismatches. The mismatches are mostly found in experiments in which axial motion was

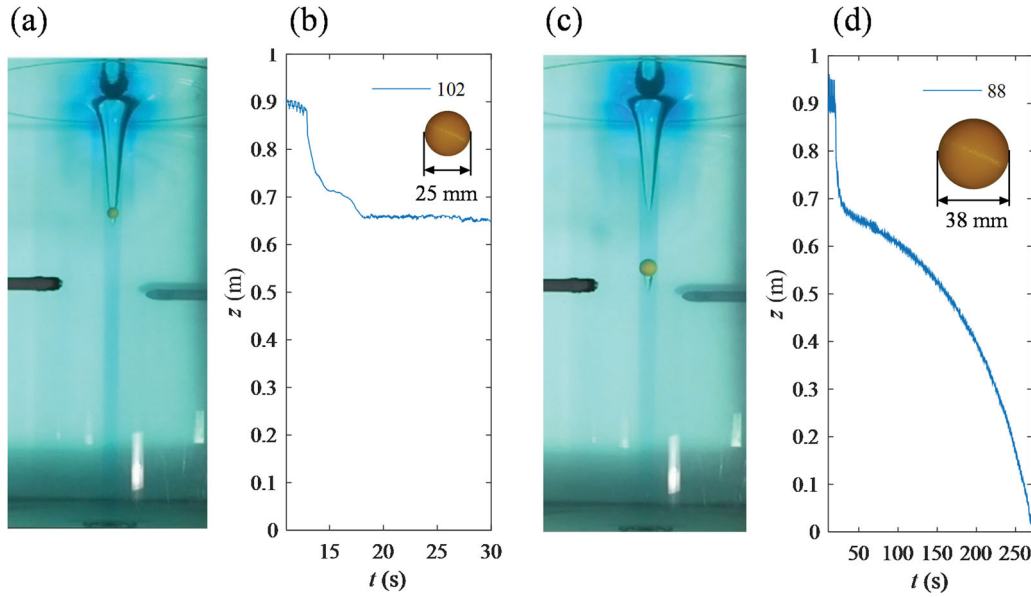


Figure 11 Recordings of axial motion along the vortex core. (a, b) $\varnothing 25$ mm sphere labelled as “No motion” with $N_{D,Taylor} \approx N_B$ (termination condition no. 2). (c, d) $\varnothing 38$ mm sphere labelled as “Indecisive motion” with $N_{D,Taylor} > N_B$ but $t_a > T$

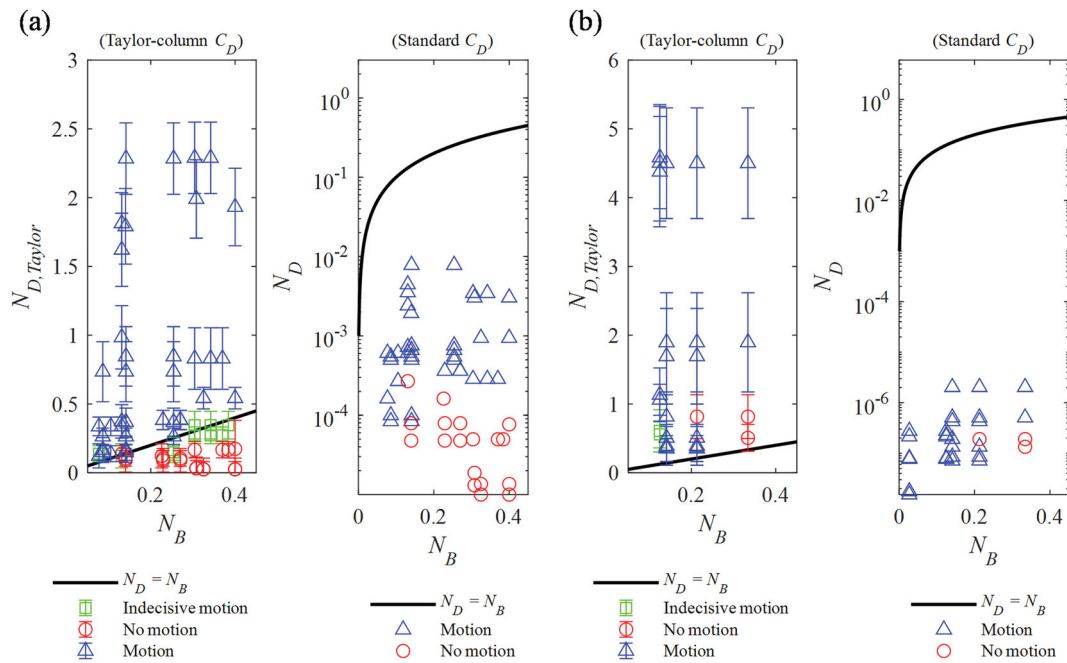


Figure 12 (a) Experimental and theoretical results for axial motion of cubes and spheres. Left: $N_{D,Taylor}$ versus N_B with $N_{D,Taylor}$ based on $C_{D,Taylor}$. Right: $N_{D,sdc}$ versus N_B with $N_{D,sdc}$ based on the standard C_D . (b) Results for axial motion of ovoids. Left: $N_{D,Taylor}$ versus N_B . Right: $N_{D,sdc}$ versus N_B

observed and labelled as “Indecisive motion”. The physical process explaining this dynamics is the recovery of the axial flow field after the field is disturbed when placing particles at the air core’s tip. This initiates an instantaneous increase in the axial velocity field in the vortex core which brings the particle in motion. Explanations on why $N_{D,Taylor}$ differs from observations may be found in the assumptions made: (1) Eq. (33) is valid for spheres. To apply Eq. (33) for non-spherical objects, Eq. (33) is proportionally adapted with the shape correction factor k . A study of Tanzosh and Stone (1994) however, showed

that for Taylor numbers $T_a > \sim 10^3$, the drag is determined by the cross-sectional area of the particle where the shape is less important and thus $k = 1$ for non-spherical objects. In the present study T_a is in the range between $\sim 3 \cdot 10^3$ and $\sim 7 \cdot 10^4$; therefore, the influence of shape is expected to be negligible. On the other hand, the results of Tanzosh and Stone (1994) are valid for Stokes flow, where in this study $\sim 10^2 < R_{p,z} < \sim 6 \cdot 10^3$ implying the Stokes condition is not met. Consequently, the effect of non-spherical shapes on the Taylor drag is not clear at this stage. (2) Equation (33) is determined for a

full solid-body rotating fluid, while in this study the vortex core is assumed to be a solid-body rotation to a large extent (due to the presence of radial diffusion of vorticity, this assumption is known not to be 100% valid). Furthermore, the solid-body field is limited to a radial range of $r \sim r_c$. Thus and with $L > 2r_c$, a part of the particle is located outside the solid-body region. The influence on the validity of Eq. (33) is then unclear. (3) The Taylor drag on a body is affected by the bounded geometry of any experimental set-up. When the set-up is axially bounded instead of a free-surface, the fluid in the Taylor column is pushed into an Ekman layer presented on this boundary and increases the drag by $\sim 50\%$ (Moore & Saffman, 1968). In this study, the outlet at the bottom is assumed to act as an unbounded condition, so bounding effects are neglected. To conclude and for $L \leq \sim 2r_c$, the stage 2 motion condition indicates if downward motion occurs.

5 Conclusions

Extensive experiments are conducted in a $\text{\O}600$ mm vortex tank to study the free-surface vortex flow driven motion of buoyant particles. The experimental particles are spherical, cubical and ellipsoid shaped with a characteristic dimension L of 0.02 to 0.04 m and the Reynolds particle number is $\sim 10^2 < \text{R}_p < \sim 10^4$. The experiments revealed that the particle's motion has a very sensitive dependence on the particle's initial conditions by showing chaotic behaviour. This behaviour is shown to be replicated in a simplified model of the particle's motion. By quantification of the LLE, the similarity in dynamics between model and experiments was shown. The vortex driven particle motion has a limited forecast horizon (typically ~ 10 s). In spite of the comprehensive set of data gathered for this study, it was not possible to formulate a criterion based on the characteristics of a vortex and a particle to predict chaotic/non-chaotic dynamics. A more extensive experimental programme would need to be in place to achieve this.

For the axial motion inside the vortex core, the results showed that this motion is determined by (un)balance between the buoyancy force and the drag force. The application of the uniform drag force with standard drag coefficients C_D is insufficient to model the axial drag force in the vortex core as the results do not match with experimental results. The C_D in this vortex core seems to be determined by the presence of a Taylor column under the particle. The $C_{D,Taylor}$ is then a function of the vortex core angular speed Ω which is a function of the vortex characteristics Γ_∞ , r_c , V_z and L . For $L \leq \sim 2r_c$ and verified with experimental data, a motion condition is proposed that indicates if downward motion inside the vortex core occurs.

To improve the reliability of the model and motion parameter Φ , the validity of the hydrodynamic forces and torque generation acting on a sphere in both irrotational and rotational rotating flows with $\text{R}_p > \sim 10^3$ and $\kappa > 1/12L$ are a subject to further study. However, there are several other processes

influencing the particle motion, e.g. the particle's influence on the surrounding flow field, the curved water–air interface, surface tension, temperature, etc. which are also subject to further study. Furthermore and to improve the accuracy of the stage 2 motion condition, the validity of Maxworthy's expression of C_D (Eq. 33) for non-spherical bodies and for bodies with $L > \sim 2r_c$ is a subject to further study.

Funding

This experimental research work is financed by the Municipality of Rotterdam, the Netherlands, Deltares and the Dutch Ministry of Economic Affairs.

Notation

a	= particle radius (m)
A_N	= cross-sectional area normal to flow (m^2)
A_S	= particle surface area (m^2)
C_A	= added mass coefficient (–)
C_D	= drag coefficient (–)
C_L	= lift coefficient (–)
C_T	= torque coefficient (–)
g	= gravitational constant (m s^{-2})
H	= undisturbed water depth above outlet (m)
H_D	= total surface depression or air core depth (m)
I_p	= particle moment of inertia (kg m^2)
L	= characteristic particle dimension (m)
Q	= flow rate ($\text{m}^3 \text{s}^{-1}$)
r	= radial coordinate (m)
r_c	= vortex core radius (m)
R_o	= Rossby number (–)
R_p	= particle Reynolds number (–)
t	= time (s)
T_p	= torque on particle (N m)
U	= particle velocity field
U_r	= particle radial velocity (m s^{-1})
U_z	= particle axial velocity (m s^{-1})
U_θ	= particle tangential velocity (m s^{-1})
V	= flow velocity field
V_r	= radial velocity (m s^{-1})
V_z	= axial velocity (m s^{-1})
V_θ	= tangential velocity (m s^{-1})
x	= x coordinate (m)
y	= y coordinate (m)
$X_{p,0}$	= particle initial conditions field
z	= axial coordinate (m)
γ	= relative velocity parameter (–)
θ	= azimuthal coordinate (rad)
λ	= Lyapunov exponent (s^{-1})
ν	= kinematic viscosity ($\text{m}^2 \text{s}^{-1}$)
ρ_f	= fluid density (kg m^{-3})
ρ_p	= particle density (kg m^{-3})

τ	= viscous stress (N m^{-2})
ω	= vorticity (s^{-1})
Γ	= circulation ($\text{m}^2 \text{s}^{-1}$)
Φ	= stage 1 motion parameter (–)
χ	= particle volume (m^3)
Ω	= angular velocity (rad s^{-1})
Ω_p	= particle angular velocity (rad s^{-1})

ORCID

Francois Clemens  <http://orcid.org/0000-0002-5731-0582>

References

- Auton, T. R. (1987). The lift force on a spherical body in a rotational flow. *Journal of Fluid Mechanics*, 183, 199–218. doi:10.1017/S002211208700260X
- Auton, T. R., Hunt, J. C. R., & Prud'homme, M. (1988). The force exerted on a body in inviscid unsteady non-uniform rotational flow. *Journal of Fluid Mechanics*, 197, 241–257. doi:10.1017/S0022112088003246
- Bagchi, P., & Balachandar, S. (2002). Shear versus vortex-induced lift force on a rigid sphere at moderate Re. *Journal of Fluid Mechanics*, 473, 379–388. doi:10.1017/S002211202002628
- Berklite, R. B. (1972). *Added mass of submerged objects of arbitrary shape*. Naval Postgraduate School.
- Bluemink, J. J., Lohse, D., Prosperetti, A., & Van Wijngaarden, L. (2009). Drag and lift forces on particles in a rotating flow. *Journal of Fluid Mechanics*, 1–31. doi:10.1017/S0022112009991881
- Burgers, J. M. (1948). A mathematical model illustrating the theory of turbulence. *Advances in Applied Mechanics*, 1, 171–199. doi:10.1016/S0065-2156(08)70100-5
- Bush, J. W. M., Stone, H. A., & Bloxham, J. (1995). Axial drop motion in rotating fluids. *Journal of Fluid Mechanics*, 282, 247–278. doi:10.1017/S0022112095000139
- Bush, J. W. M., Stone, H. A., & Tanzosh, J. P. (1994). Particle motion in rotating viscous fluids: Historical survey and recent developments. *Current Topics in The Physics of Fluids*, 1, 337–355.
- Duinmeijer, S. P. A., Moreno-Rodenas, M. A., Lepot, M., Nieuwenhuizen van, C., Meyer, I., & Clemens, F. H. L. R. (2019). A simple measuring set-up for the experimental determination of the dynamics of a large particle in the 3D velocity field around a free-surface vortex. *Journal of Flow Measurement and Instrumentation*. doi.org/10.1016/j.flowmeasinst.2018.10.007
- Duinmeijer, S. P. A., Oldenzel, G., & Clemens, F. H. L. R. (2019). Experimental study on the 3D-flow field of a free-surface vortex using stereo PIV. *Journal of Hydraulic Research*. doi:10.1080/00221686.2018.1555558
- Fukada, T., Takeuchi, S., & Kajishima, T. (2014). Effects of curvature and vorticity in rotating flows on hydrodynamic forces acting on a sphere. *International Journal of Multiphase Flow*, 58, 292–300. doi:10.1016/j.ijmultiphaseflow.2013.10.006
- Gaspard, P. (2005). *Chaos, scattering and statistical mechanics*. Cambridge University Press. ISBN: 978-0521018258.
- Holzer, A., & Sommerfeld, M. (2008). New simple correlation formula for the drag coefficient of non-spherical particles. *Powder Technology*, 184(3), 361–365. doi:10.1016/j.powtec.2007.08.021
- Maxworthy, T. (1970). The flow created by a sphere moving along the axis of a rotating, slightly-viscous fluid. *Journal of Fluid Mechanics*, 40(3), 453–479. doi:10.1017/S0022112070000265
- Mei, R. (1992). An approximate expression for the shear lift force on a spherical particle at finite Reynolds number. *International Journal of Multiphase flows*, 18(1), 145–147. doi:10.1016/0301-9322(92)90012-6
- Moore, D. W., & Saffman, P. G. (1968). The rise of a body through a rotating fluid in a container of finite length. *Journal of Fluid Mechanics*, 31(4), 635–642. doi:10.1017/S0022112068000376
- Moore, D. W., & Saffman, P. G. (1969). The structure of free vertical shear layers in a rotating fluid and the motion produced by a slowly rising body. *Philosophical Transactions of the Royal Society of London. Series A, Mathematical and Physical Sciences*, 264(1156), 597–643. doi:10.1098/rsta.1969.0036
- Powell, M. J. D. (1970). *A fortran subroutine for solving systems of nonlinear algebraic equations*. Numerical Methods for Nonlinear Algebraic Equations, Ch.7.
- Proudman, J. (1916). On the motion of solids in a liquid possessing vorticity. *Proceedings of the Royal Society of London. Series A, Containing Papers of a Mathematical and Physical Character*, 92(642), 408. doi:10.1098/rspa.1916.0026
- Roenby, J., & Aref, H. (2010). Chaos in body-vortex interactions. *Proceedings of the Royal Society A: Mathematical, Physical and Engineering Sciences*, 466(2119), 1871–1891. doi:10.1098/rspa.2009.0619 doi:10.1098/rspa.2009.0619
- Rosenstein, M. T., Collins, J. J., & DeLuca, C. J. (1993). A practical method for calculating the largest Lyapunov exponents from small data sets. *Physica D: Nonlinear Phenomena*, 65(1-2), 117–134. doi:10.1016/0167-2789(93)90009-P
- Saffman, P. G. (1965). The lift on a small sphere in a slow shear flow. *Journal of Fluid Mechanics*, 22(2), 385–400. doi:10.1017/S0022112065000824
- Saffman, P. G. (1968). Corrigendum to “The lift on a small sphere in a slow shear flow”. *Journal of Fluid Mechanics*, 31(3), 624. doi:10.1017/S0022112068999990
- Stewartson, K. (1952). On the slow motion of a sphere along the axis of a rotating fluid. *Proceedings of the Cambridge Philosophical Society*, 48(1), 168–177. doi:10.1017/S0305004100027468

- Tanzosh, J. P., & Stone, H. A. (1994). Motion of a rigid particle in a rotating viscous flow: An integral equation approach. *Journal of Fluid Mechanics*, 275, 225–256. doi:10.1017/S002211209400234X
- Taylor, G. I. (1917). Motion of solids in fluids when the flow is not irrotational. *Proceedings of the Royal Society of London. Series A, Containing Papers of a Mathematical and Physical Character*, 93(648), 99–113. doi:10.1098/rspa.1917.0007
- Tio, K.-K., Liñán, A., Lasheres, J. C., & Gañan-Calvo, M. (1993). On the dynamics of buoyant and heavy particles in a periodic Stuart vortex flow. *Journal of Fluid Mechanics*, 254, 671–699. doi:10.1017/S0022112093002307
- Van Nierop, E. A., Luther, S., Bluemink, J. J., Magnaudet, J., Prosperetti, A., & Lohse, D. (2007). Drag and lift forces on bubbles in a rotating flow. *Journal of Fluid Mechanics*, 571, 439–454. doi:10.1017/S0022112006003387
- Voßwinkel, N. (2017). Transportvermögen von Einlaufwirbeln [Transport capacity of free-surface vortices], Band: 21, Reihe: Bericht-Lehr- und Forschungsgebiet Wasserwirtschaft und Wasserbau, ISBN 978-3-8440-5242-8. Shaker Verlag GmbH Germany.
- Westerweel, J., & Scarano, F. (2005). Universal outlier detection for PIV data. *Experiments in Fluids*, 39(6), 1096–1100. doi:10.1007/s00348-005-0016-6